Chemical Geology 662 (2024) 122214

Contents lists available at ScienceDirect

Chemical Geology

journal homepage: www.elsevier.com/locate/chemgeo

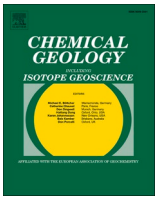

Reconstructing the depositional environment and diagenetic modification of global phosphate deposits through integration of uranium and strontium isotopes

Robert C. Hill [a], Zhen Wang [a,b], Gordon D.Z. Williams [a], Victor Polyak [c], Anjali Singh [d], Michael A. Kipp [a], Yemane Asmerom [c], Avner Vengosh [a,*]

[a] Nicholas School of the Environment, Duke University, Durham, NC 27708, USA
[b] School of Earth, Atmosphere & Environment, Monash University, Clayton, VIC 3800, Australia
[c] Earth and Planetary Sciences, University of New Mexico, Albuquerque, NM 87131, USA
[d] Department of Geology, Mohanlal Sukhadia University, Udaipur, Rajasthan 313001, India

ARTICLE INFO

Editor: Christian France-Lanord

Keywords:
Phosphate rocks
Uranium
Strontium
Isotope
Carbonate-fluorapatite

ABSTRACT

The geochemistry of phosphate rocks can provide valuable information on their depositional environment and the redox condition of global oceans through time. Here we examine trace metal concentrations and uranium ($\delta^{238}U$, $\delta^{234}U$) and strontium ($^{87}Sr/^{86}Sr$) isotope variations of marine sedimentary phosphate rocks and the phosphate-bearing carbonate fluorapatite (CFA) mineral phase, originating from Precambrian to mid-Miocene aged major global phosphate deposits. We find elevated concentrations of several trace elements (Al, V, Cr, Cd, U, Mn, Co, Cu, As, and Rb) in the CFA mineral phase of young phosphate rocks (Miocene to Late Cretaceous) relative to those of older (Devonian to Precambrian) rocks. The $\delta^{238}U$ of phosphate rocks of Mid-Miocene to Permian age range from −0.311‰ to 0.070‰, exhibiting a positive fractionation relative to modern seawater (−0.38‰). This is similar to the isotope fractionation reported for carbonate and shale sediments, likely resulting from the reduction of uranium in porewaters during CFA precipitation. Cambrian to Precambrian phosphate rocks have lower $\delta^{238}U$ of −0.583‰ to −0.363‰, indicating different depositional redox conditions likely resulting from seafloor anoxia and/or diagenetic modification. The $^{87}Sr/^{86}Sr$ ratios of phosphate rocks of Cretaceous to Mid-Miocene age generally follow the secular $^{87}Sr/^{86}Sr$ seawater curve. Phosphate rocks with $^{87}Sr/^{86}Sr$ that deviate from this curve have characteristic trace metal trends, such as lower Sr/Ca and Sr concentrations, suggesting later diagenetic modification. Older phosphate rocks of Precambrian age are systematically more radiogenic than the expected secular Sr seawater composition at the time of deposition, possibly due to the greater influence of terrestrial input in peritidal zones and/or more pervasive diagenetic modification. Overall, our study reveals connections between U and Sr isotope variations for reconstructing the depositional and diagenetic conditions of global phosphate rock formation through Earth history and the transition to an oxic ocean following the Paleozoic Oxygenation Event.

1. Introduction

Phosphate rocks (PRs) were deposited around the world during intervals of global environmental change (Papineau, 2010). The geochemistry of these PRs can potentially be used to reconstruct major geological events in Earth history, including changes in seawater redox conditions and diagenetic environments. Previous work has determined that phosphogenesis typically occurs in shallow continental shelf-slope settings under suboxic-to-anoxic porewater conditions (Filippelli, 2011). Upwelling of nutrient-rich bottom water is thought to be the major source for phosphorus (P), which is supplied to the seafloor via the biological pump. Accumulation of biogenic P in organic-rich sediments, followed by its bacterially-mediated release into porewaters (Schulz and Schulz, 2005), results in the precipitation of carbonate-fluorapatite (CFA) during early diagenesis (Pufahl and Groat, 2017). Co-enrichment of redox-sensitive elements (e.g., U) in CFA (Altschuler, 1980) is consistent with anoxic porewater conditions, as is the common co-occurrence of glauconite (Fe/Mn-rich phyllosilicate), pyrite, and

* Corresponding author.
E-mail address: vengosh@duke.edu (A. Vengosh).

https://doi.org/10.1016/j.chemgeo.2024.122214
Received 27 February 2024; Received in revised form 5 June 2024; Accepted 7 June 2024
Available online 12 June 2024

dolomite (Pufahl and Groat, 2017).

Important differences in depositional settings and processes have been proposed between Proterozoic and Phanerozoic PRs (Pufahl and Groat, 2017). For Phanerozoic-aged PRs, deposition primarily occurred in continental shelf environments, whereas Proterozoic-aged deposits were predominantly formed in peritidal settings (Pufahl and Groat, 2017). Furthermore, deposition of Phanerozoic P-rich horizons was often followed by winnowing and reworking (Filippelli, 2011), which is not as apparent in Proterozoic deposits. Lastly, during the Proterozoic Eon, it has been suggested that (i) organic matter (and associated P) remineralization was muted (Kipp and Stueken, 2017), and that (ii) dissolved P was perhaps adsorbed onto Fe and/or Mn oxides and shuttled to the seafloor, followed by dissolution in anoxic porewaters to enable CFA precipitation (Pufahl and Groat, 2017). In sum, this implies alternative P supply pathways in a dominantly anoxic Precambrian Ocean. For these reasons, we propose using the U and Sr isotope geochemical proxies to reconstruct the depositional (e.g., redox) conditions of Proterozoic and Phanerozoic PRs and to distinguish depositional from diagenetic modifications.

Previous studies have suggested that PRs can record the $^{87}Sr/^{86}Sr$ ratio of pore water in the early diagenetic stages of phosphate formation, which is assumed to be identical to the composition of contemporaneous seawater (Compton et al., 1993; Mallinson et al., 1994; McArthur et al., 1990). Generally, CFA in Modern PR deposits have $^{87}Sr/^{86}Sr$ ratios similar to that of both modern seawater and porewaters (Kolodny and Luz, 1992). Yet, in many cases, the $^{87}Sr/^{86}Sr$ ratios of PRs have been reported to be higher (i.e., more radiogenic) than the contemporaneous $^{87}Sr/^{86}Sr$ seawater values, suggesting another influence (Kolodny and Luz, 1992; Soudry et al., 2006; Soudry and Yaacov, 2005). Elevated Sr concentrations and high Sr/Ca ratios have been associated with marine $^{87}Sr/^{86}Sr$ ratios in PRs, while late diagenetic modification of apatite by freshwater exposure has been inferred from lower Sr/Ca ratios and higher $^{87}Sr/^{86}Sr$ (McArthur et al., 1987).

The "stable" uranium isotope ratio ($^{238}U/^{235}U$, expressed as $\delta^{238}U$, defined as the permil variation of sample ratio from that of a standard) has been used to investigate the carbonate record through geological time (Chen et al., 2018; Romaniello et al., 2013), namely for the reconstruction of ocean paleo-redox conditions (Chen et al., 2021; Zhang et al., 2020). The ability to use $\delta^{238}U$ for paleo-redox reconstruction lies in the redox sensitivity of U. In oxidizing conditions, U exists as soluble U(VI), while in reducing environments U becomes insoluble U(IV) and is sequestered in sediments. In PRs, the reduction of U(VI) to U(IV) is the primary mechanism by which U is incorporated into CFA, with it structurally fixed in substitution of Ca, although post depositional oxidation and sorption processes can produce and incorporate U as U(VI) (Altschuler et al., 1958). Reduced sediments are thus enriched in U, and also in ^{238}U relative to ^{235}U (e.g., the Black Sea; Rolison et al., 2017). Primary carbonates have $\delta^{238}U$ values that closely resemble ambient seawater (Kipp et al., 2022; Tissot et al., 2018; Weyer et al., 2008), meaning that they can be used to infer the $\delta^{238}U$ of the past ocean. Using isotope mass balance approach, $\delta^{238}U$ variations can be related to the extent of seafloor anoxia (Kipp and Tissot, 2022). However, such reconstructions are complicated by the fact that many carbonate sediments become positively fractionated relative to seawater due to incorporation of reduced U (Chen et al., 2018; Romaniello et al., 2013; Tissot et al., 2018; Yuan et al., 2023). Thus, other archives beyond the carbonate sediment record are needed to evaluate the redox evolution of the ocean using U isotope systematics. As far as we are aware, this study is the first to present a systematic $\delta^{238}U$ record in the PR geological archive through time.

Due to the formation of CFA in anoxic environments, we hypothesize that CFA will have a $\delta^{238}U$ higher than their ambient seawater, similar to the reported U isotope variations in carbonates deposited under reducing porewater conditions (Yuan et al., 2023). In contrast, previous studies have shown that the sorption of U onto ferromanganese sediments and nodules produces a negative $\delta^{238}U$ fractionation relative to seawater (Goto et al., 2014; Stirling et al., 2007; Weyer et al., 2008) and that non-weathered modern to Neogene dredged seafloor phosphorites have a $\delta^{238}U$ at or below modern seawater (Kolodny et al., 2017). This negative $\delta^{238}U$ fractionation could be more prevalent in Precambrian PRs that were apparently not governed by organic-rich upwelling deposits and rather inferred to have received U from adsorption onto FeMn-oxides (Pufahl and Groat, 2017). We hypothesize that the prevalence of seafloor anoxia during the Precambrian, which implies that the seawater $\delta^{238}U$ was likely much lower than modern seawater (Kipp and Tissot, 2022; Chen et al., 2021; Gilleaudeau et al., 2019), was the primary influence of lower $\delta^{238}U$ in Proterozoic PRs. Furthermore, previous studies have highlighted the enrichment of U and other redox-sensitive metal(loid)s in PRs (Altschuler, 1980). PRs have much higher U concentrations (~100 mg/kg) than biogenic carbonates (~ 1.5 mg/kg) and authigenic carbonates (~ 4.1 mg/kg) (Baturin and Kochenov, 2001; Gabriel et al., 2013; Romaniello et al., 2013; Sun et al., 2020).

In contrast to the "stable" U isotope systematics, the radiogenic U isotope ratio $^{234}U/^{238}U$ (expressed as $\delta^{234}U$, the permil deviation of the atomic $^{234}U/^{238}U$ ratio of a sample relative to the secular equilibrium ratio [equal to the ratio of their half-lives]) reflects the ^{234}U enrichment over the secular equilibrium value ($\delta^{234}U = 0‰$). If a system has been closed (i.e. no loss or gain of U) for longer than ~2 million years, i.e., 8 times the half-life of ^{234}U (245,620 yr; Cheng et al., 2013), secular equilibrium is reached and maintained ($\delta^{234}U \sim 0‰$). Thus, any deviation from a $\delta^{234}U$ of 0‰ indicates U alteration within the past 2 million years, meaning radiogenic U isotope systematics can be used to assess recent alterations of sedimentary rocks.

Here, we report the first dataset combining trace elements concentrations, $\delta^{238}U$, and $^{87}Sr/^{86}Sr$ in PRs originating from the major global phosphate deposits from the Precambrian to mid-Miocene, including sedimentary PRs from the U.S., Peru, Senegal, Togo, Western Sahara, Morocco, Algeria, Tunisia, Israel, Syria, Jordan, Egypt, India, and China. Most of the PR samples in this study were collected opportunistically from active phosphate mines and thus lack precise geological context and radiometric age constraints. Geological age estimates were based on the known ages of the hosting geological formations. Through a sequential leaching process, we characterized the occurrence of U and Sr in the different mineral phases within the PRs and determined their U and Sr isotope variations. In addition, X-ray diffraction was used to verify mineralogical phases in the PRs. The objective of this study is to use this unique dataset of integrated trace elements, $\delta^{238}U$, $\delta^{234}U$, and $^{87}Sr/^{86}Sr$ in marine PRs for the reconstruction of the paleo-depositional setting of global phosphate formations and/or their possible diagenetic modifications through geological time.

2. Materials and analytical methods

2.1. Sample collection and preparation

Samples were collected directly from phosphate mines and archives at the Julius Kühn Institute in Germany (Table S1) (Sattouf et al., 2008; Sattouf et al., 2007; Sun et al., 2020). Information on the source of the ores is provided in the literature (Table S1) and the U.S. Geological Survey dataset of the world phosphate mines (Chernoff and Orris, 2002). The sample collection in this study includes 70 sedimentary PRs from major PR producing countries (e.g., China, Morocco, U.S.) of ages from Middle Miocene to Paleoproterozoic. In addition, 11 magmatic PRs were also analyzed (Table S2).

Prior to laboratory analysis, each sample was oven-dried at 50 °C until reaching a constant weight and was passed through a 2-mm sieve for homogenization. A subset of sample, by coning and quartering, was ground using a ceramic mortar and pestle to pass through a 200-mesh stainless steel sieve. All PR samples were fully digested through a HF-HNO_3 mixture (Vengosh et al., 2019; Wang et al., 2023); subsets of samples were also digested via HCl (6 N) (Bartlett et al., 2018) and sequential leaching methods (Section 2.3). The efficiency of digestion

and accuracy of measurements were assessed by repeated digestion and measurement of the Natural Moroccan PR IRMM BCR-032. This yielded recoveries within 10% of certified standard values for Mg, P, Ca, V, Cr, Ni, Cu, Cd, and U; and within 20% of certified standard values for Al, Mn, Fe, Co, and As (Table S3).

2.2. X-ray diffractometry

A subset of samples was measured via x-ray diffraction (XRD) on a Pananalytical X'Pert PRO diffractometer with CuKα radiation at the Duke University Shared Materials Instrumentation Facility (SMIF). The XRD was operated at 45 kV and 40 mA with a ½ degree fixed divergent slit, 10 mm beam mask, and 0.04 rad soller slit. The data collection range was 2θ 10 to 80 with a 0.05° step size and a 3° per minute scan rate. Coarse samples were crushed into a fine powder with a mortar and pestle and secured onto an amorphous glass slide prior to analysis.

2.3. Sequential leaching experiments

A sequential leach method was used to assess the chemical and isotopic composition of the carbonate (often dolomitic) and CFA phases of PR samples (Gupta and Chen, 1975; Hass and Fine, 2010; Stewart et al., 2015). Utilizing a 30:1 liquid to solid ratio (mL:g), samples were leached in 1 M ammonium acetate (NH_4Ac) buffered to pH 8, followed by 1 M acetic acid (HOAc) and 1 M HCl to isolate the exchangeable cations and the carbonate and phosphate fractions, respectively. These latter fractions were subsequently analyzed for trace metals and $^{87}Sr/^{86}Sr$. Efficacy of the procedure was demonstrated by nearly complete recovery (mean = 88%) of phosphorus (P) and a strong relationship between calcium (Ca) and P ($\rho = 0.93$, $p < 0.01$) in the phosphate fraction, confirming selective leaching of the CFA phase (Figs. S1-S2) due to Ca and P being the primary elements in the CFA mineral.

2.4. Analytical measurements

Trace metals were measured on an inductively coupled plasma mass spectrometer (ICP-MS, Thermo Fisher X-Series II) at Duke University, equipped with a collision/reaction cell device. An aliquot of digestant was dried down and redissolved in 7 N HNO_3 to gather 1–2 μg of Sr. Strontium was isolated via ion-exchange chromatography with a Sr-specific resin (Eichrom®). The $^{87}Sr/^{86}Sr$ isotope ratio of samples were measured in positive ion mode on a ThermoFisher Triton thermal ionization mass spectrometer (TIMS) at Duke University. NIST SRM 987 was analyzed repeatedly to demonstrate analytical reproducibility and yields a value of 0.710255 ± 0.000010 ($n = 58$).

Uranium was isolated by ion-exchange chromatography using Bio-Rad AG® 1-X8 Resin in preparation for isotope analysis (Polyak et al., 2023). Eluted samples were dried down and dissolved in 3% HNO_3 for U isotope analysis on a Thermo Neptune multi-collector ICP-MS at the University of New Mexico Albuquerque Radiogenic Isotope Lab. A spiked NBL-112A (CRM-112A) standard was analyzed and yielded a value of 137.83 ± 0.01 ($n = 19$) (Polyak et al., 2023), which is consistent with the adjusted standard value of 137.837 ± 0.015 (Richter et al., 2010). $^{238}U/^{235}U$ and $^{234}U/^{238}U$ are reported in delta notation as defined in (1) and (2) below.

(1)

$$\delta^{238}U\ (‰) = \left[\frac{\left(^{238}U/^{235}U\right)_{sample}}{\left(^{238}U/^{235}U\right)_{CRM112A}} - 1\right] \times 1000$$

(2)

$$\delta^{234}U\ (‰) = \left[\left(^{234}U/^{238}U\right)_{Activity} - 1\right] \times 1000$$

2.5. Statistical analyses

All statistical calculations and analyses were performed in R (v 4.3.0) (R Core Team, 2023; Xu et al., 2021). Nonparametric analyses were conducted, including the Mann-Whitney test and Spearman's rank correlation test where Rho (ρ) evaluates the strength of the correlation. Statistical significance is based on p values, where $p < 0.01$ for a 99% confidence interval and $p < 0.05$ for a 95% confidence interval. The coefficient of determination (r^2) is used to assess the linearity of a modeled fit line for data that passes a Shapiro-Wilk normativity test with $p > 0.05$.

3. Results

3.1. Mineralogy and geochemistry

The combined chemical (Table 1) and XRD data indicate that the predominant mineral in most analyzed PRs is CFA. Although most Miocene to Late Cretaceous PRs (hereafter referred to as "young" PRs) contain primarily CFA, other minerals have been identified, including low (<5%) to moderate (5–25%) occurrences of quartz, dolomite (mid-Miocene), and major amounts of (>25%) calcite (Late Cretaceous PRs from Israel) (Table S4). PRs from China (Late Devonian to Neoproterozoic) contain lower proportions of CFA than the younger samples, moderate to major amounts of quartz, and many of the Neoproterozoic PRs contain moderate amounts of dolomite or ankerite. Paleoproterozoic PRs from India were found to contain a variety of mineral compositions: three of the six analyzed rocks contain >90% CFA and minor amounts of quartz; with one of the three also containing minor amounts of goethite and dolomite. The remaining three each contain major amounts of either dolomite, quartz, or goethite. The data show a positive correlation between CFA abundance and P_2O_5 concentrations in PRs ($\rho = 0.66$, $p < 0.01$, Fig. S3).

Among all the analyzed PRs, there are strong relationships between aluminum (Al) and rubidium (Rb), ($\rho = 0.78$), as well as potassium (K) and Rb ($\rho = 0.89$, Fig. S4). This suggest that the occurrence of Rb in PRs may be due to the incorporation of potassium-rich aluminosilicate clays (Chen et al., 2022). This is further supported by the minimal incorporation of these elements in the extracted CFA phase (Fig. 1F:H, Table S5-S6). Sequential leach experiments show that in comparison to bulk digest data, P, Ca, Sr, U, and rare earth elements and yttrium (REY) primarily incorporate into the phosphate (CFA) phase ($n = 38$) (Fig. 1A:E). Although REYs are completely derived from the CFA phase, Eocene PRs from Senegal are notably depleted in light rare earth elements (LREE) (Table S6).

Precambrian PRs with high Rb may have their Sr isotope signatures overprinted by ^{87}Rb decay, which further establishes the need for targeted analysis of the phosphate-bearing phases. Young PRs are generally more enriched in vanadium (V), chromium (Cr), cadmium (Cd), and U compared to older samples (Cambrian to Precambrian) ($p < 0.01$; Table 2). Notably, some Mid-Permian PRs from the U.S. are also characterized by elevated concentrations of these elements (Table 2). Combined, these elements are redox-sensitive metal(loid)s often used as paleoredox proxies (Tribovillard et al., 2006).

3.2. Uranium isotopes

A total of 27 sedimentary (and 3 magmatic, Table S2) PR samples were selected for uranium isotope analysis. The $\delta^{238}U$ values of measured young PRs fall within a range of −0.311‰ to −0.102 ‰ ($n = 16$) (Table 1, Fig. 2A). Uranium concentrations of the young PRs varied considerably from 37 to 154 mg/kg ($n = 44$; Table 2). Mid-Permian PRs are within similar ranges of $\delta^{238}U$ (−0.160 to 0.070 ‰; $n = 3$) and U

Table 1
Elemental and Isotopic compositions of phosphate rocks from the United States (US), Peru (PE), Senegal (SN), Togo (TG), Algeria (DZ), Tunisia (TN), Morocco (MA), Western Sahara (EH), Israel (IL), Syria (SY), Jordan (JO), Egypt (EG), China (CN), and India (IN). P_2O_5 is given in units of wt% and other elemental data is given as mg/kg.

Sample	Age	P_2O_5	Na	Mg	Al	K	Ca	V	Cr	Mn	Rb	Sr	Mo	Cd	U	$^{87}Sr/^{86}Sr$	$\delta^{238}U$	$\delta^{234}U$
US_1	Middle Miocene	27.0	7401	12,024	5077	2204	328,112	93.2	39.6	162	10.9	1113	10.8	1.69	154	0.708919	−0.237 ± 0.024	−8.06 ± 6.16
US_2	Middle Miocene	31.3	3464	1237	3599	712	303,847	65.9	70.9	339	4.21	710	5.27	23	97.4	0.708611		
US_3	Middle Miocene	32.4	5502	1827	3980	914	297,612	92.4	56.8	158	6.15	1043	7.27	4.65	105	0.708847	−0.231 ± 0.017	25.85 ± 7.30
US_4	Middle Miocene	32.5	4007	1856	3830	1179	306,676	65.2	50	308	6.59	1046	7.9	5.44	94.9	0.708744		
US_5	Middle Miocene	31.9	3121	1493	3641	955	295,395	56.2	56.3	177	5.94	1048	5.87	6.47	59.1	0.708023		
US_6	Middle Miocene	32.7	3376	1113	4198	666	302,266	56.2	66	194	4	811	2.13	11.9	88.9	0.708653		
US_7	Middle Miocene	35.7	3254	1520	5346	900	309,678	88.6	55.1	253	5.49	656	4.89	19	110	0.708774		
US_8	Middle Miocene	34.4	6855	2037	6802	1123	322,604	91.7	54.8	317	7.87	1076	6.46	5.9	136	0.708897	−0.311 ± 0.032	39.03 ± 6.76
US_9	Middle Miocene	34.6	2908	846	3648	566	292,206	58.2	53.5	96.7	3.96	618	1.73	10.8	96.4	0.708734		
US_10	Middle Miocene	33.5	2887	1061	4092	692	291,942	78.0	45	192	4.58	519	6.91	13.1	128	0.708850		
US_11	Middle Miocene	31.3	6268	2993	1999	909	336,847	26.5	152	25.5	4.79	2534	8.57	33.6	61.9	0.708489	−0.133 ± 0.028	22.90 ± 8.58
PE_1	Middle Miocene	32.3	12,621	3300	3655	1639	310,590	62.2	153	83.4	6.64	2305	5.95	42	64.1	0.708860	−0.188 ± 0.029	17.05 ± 6.60
SN_1	Eocene	43.2	404	146	3142	119	327,453	347	114	690	0.42	348	0.771	32.3	105	0.708650		
SN_2	Eocene	35.1	1006	202	3610	92.9	304,017	264	173	280	0.378	1253	4.35	106	84.6	0.706628		
SN_3	Eocene	35.0	946	206	5240	58.6	306,862	183	133	295	0.598	677	2.23	68.9	79.7	0.707903		
TG_1	Eocene	35.5	1794	565	3233	332	326,081	57.5	99.4	191	2.43	417	5.22	52	90.7	0.707105	−0.104 ± 0.033	15.81 ± 6.41
TG_2	Eocene	34.7	1740	555	3015	295	305,031	59.9	101	259	2.3	392	14	52.1	99.4	0.707263		
TG_3	Eocene	36.4	1789	551	4178	314	314,507	60.3	95.7	418	2.15	394	10.1	52.7	88.4	0.707257		
DZ_1	Eocene	27.4	8740	8011	2529	1135	332,555	52.9	221	18.4	4.09	2116	2.35	25.2	51.1	0.707869		
DZ_2	Eocene	28.7	9109	7970	2209	1170	341,343	51.3	212	20.6	3.97	2129	3.02	22.3	49	0.707860		
DZ_3	Eocene	28.8	8226	8741	2073	1899	296,278	46.4	193	20.6	3.73	1808	2.11	21.9	41.3	0.707862		
TN_1	Late Paleocene	26.1	8592	3050	1452	535	328,974	46.7	161	13.5	2.22	1853	7.22	66.7	44.3	0.707854	−0.239 ± 0.023	0.96 ± 10.97
TN_2	Late Paleocene	29.7	8231	4478	1360	581	321,941	47.1	162	14.1	2.25	1809	4.25	44.8	37.1	0.707853		
TN_3	Late Paleocene	29.5	9781	3004	1503	601	358,843	51.5	182	13.2	2.41	2051	4.16	57.3	45.3	0.707836		
MA_1	Paleocene	33.3	5135	2042	2209	663	335,465	145	245	16.1	3.03	881	2.68	20.8	114	0.707907	−0.155 ± 0.034	0.13 ± 6.32
MA_2	Paleocene	40.6	5760	2837	2838	772	336,948	203	286	10.9	3.88	978	1.16	11.9	126	0.707924	−0.162 ± 0.024	−4.37 ± 7.52
MA_3	Paleocene	34.1	5620	1706	1728	663	359,361	145	342	4.93	3.6	878	2.64	8.67	110	0.707911		
MA_4	Paleocene	18.9	5537	3132	1426	586	327,490	161	215	10.3	2.28	1000	4.38	17.9	106	0.707923	−0.133 ± 0.076	−1.40 ± 13.52
MA_5	Paleocene	31.8	5197	1989	1484	308	336,680	162	258	6.93	1.04	984	2.85	2.43	79.8	0.707555		
MA_6	Paleocene	30.5	4849	3460	2369	969	316,874	142	302	19.5	3.76	870	1.78	11.2	114	0.707938		
EH_1	Paleocene	33.9	1011	505	2206	1019	310,532	83.2	115	32.7	3.82	256	1.99	40.8	59.7	0.708913		
IL_1	Late Cretaceous	26.0	4181	977	1178	127	338,803	116	110	13.3	0.672	1078	10.9	23.1	105	0.707827	−0.119 ± 0.033	−9.50 ± 7.47
IL_2	Late Cretaceous	22.6	6676	1114	1054	57.5	327,403	55.0	107	20.8	0.412	1005	2.75	19	65.8	0.707854		
IL_3	Late Cretaceous	34.3	4821	1305	960	166	338,070	138	140	6.67	0.592	1488	1.97	8.54	117	0.707764	−0.119 ± 0.032	−2.16 ± 7.63
IL_4	Late Cretaceous	34.0	3962	1479	1493	187	338,295	93.6	131	1.57	1.01	1472	2.2	18.8	99.4	0.707731		
IL_5	Late Cretaceous	38.0	4645	1310	723	170	340,741	156	53.8	10.8	0.348	2718	18.8	18.9	106	0.707773	−0.120 ± 0.019	−3.39 ± 7.98
IL_6	Late Cretaceous	32.1	3759	1493	714	82	354,301	104	124	3.42	0.195	1846	7.71	2.75	79.3	0.707769	−0.241 ± 0.037	4.37 ± 7.19
IL_7	Late Cretaceous	32.3	6259	1245	384	167	332,420	146	119	6.38	0.291	1882	3.9	14.9	117	0.707768	−0.102 ± 0.044	18.48 ± 7.27
IL_8	Late Cretaceous	33.6	5859	1262	396	180	335,601	172	131	5.16	0.543	1936	5.43	15.4	125	0.707765		
SY_1	Late Cretaceous	24.6	3451	13,560	1851	387	290,556	141	258	21.9	1.94	1232	4.88	5.4	42.7	0.707764		
SY_2	Late Cretaceous	30.4	2907	3832	736	208	296,408	69.5	106	5.11	1.08	1431	1.47	3.87	48.3	0.707747		
SY_3	Late Cretaceous	31.2	5304	2295	3640	2796	306,977	83.5	193	41.8	11.4	1593	0.177	0.636	114	0.707606		
JO_1	Late Cretaceous	28.9	4727	3550	1051	179	303,217	67.0	96.9	11.4	0.93	1012	2.11	7.61	52.9	0.707729	−0.181 ± 0.023	1.96 ± 8.65
EG_1	Late Cretaceous	42.4	4744	1926	4178	568	298,709	106	84.8	843	2.23	1482	5.98	7.65	68.1	0.707533		
US_12	Middle Permian	21.3	8262	1803	13,032	6832	213,847	149	593	33.3	28.4	878	23.6	112	58.2	0.708609	−0.053 ± 0.021	7.88 ± 6.27
US_13	Middle Permian	22.3	6111	679	3480	1196	235,615	113	588	18.3	5.52	622	25	0.187	75.4	0.708158		
US_14	Middle Permian	26.8	6662	1311	4267	4195	262,465	124	814	6.42	10.4	1659	14.3	2.67	91.9	0.707859		
US_15	Middle Permian	27.3	7672	1402	2451	2212	266,626	87.9	613	5.64	5.56	1713	5.35	1.91	53.5	0.707819		
US_16	Middle Permian	26.7	7450	6131	9919	3626	269,526	83.7	299	48.3	14.1	827	4.7	0.729	72.4	0.708377		
US_17	Middle Permian	26.9	1469	1457	6424	3241	252,060	1658	413	17.4	12.6	713	125	175	121	0.707650	0.070 ± 0.054	−3.30 ± 8.58
US_18	Middle Permian	27.1	1419	939	7437	3549	242,427	2645	620	8.39	14.7	686	52.3	252	114	0.707679	−0.160 ± 0.038	4.65 ± 6.78
CN_1	Devonian	28.1	562	16,708	5537	2121	287,371	89.2	42.4	261	5.19	1064	1.79	1.12	19.3	0.708047		
CN_2	Devonian	21.5	1376	23,060	975	818	250,692	27.1	93.7	171	2.47	482	2.45	0.787	12.7	0.711241	−0.250 ± 0.021	115.87 ± 8.33

(*continued on next page*)

Table 1 (*continued*)

Sample	Age	P_2O_5	Na	Mg	Al	K	Ca	V	Cr	Mn	Rb	Sr	Mo	Cd	U	$^{87}Sr/^{86}Sr$	$\delta^{238}U$		$\delta^{234}U$	
CN_3	Early Cambrian	20.0	1218	1353	8541	5900	180,446	27.0	60.8	104	15.9	804	–	0.184	17.3	0.709342				
CN_4	Early Cambrian	24.7	1077	4841	8856	7656	250,052	50.0	20.4	2592	24.3	438	7.3	1.19	19.5	0.711636	−0.472	± 0.031	−21.53	± 9.45
CN_5	Early Cambrian	23.9	928	1973	6296	4060	191,211	34.5	35.7	74.8	13.3	517	–	0.177	11.8	0.711181				
CN_6	Neoproterozoic	27.7	2870	21,992	1864	1670	335,519	9.43	7.89	106	2.16	671	1.1	0.065	6.78	0.713144				
CN_7	Neoproterozoic	24.8	3669	12,783	9145	13,011	249,626	20.4	19.2	121	15.6	652	0.362	0.14	4.2	0.711919				
CN_8	Neoproterozoic	20.4	4771	8291	15,855	15,786	209,477	30.9	63.7	125	45.1	834	1.11	0.224	2.74	0.715931	−0.553	± 0.058	115.84	± 22.13
CN_9	Neoproterozoic	30.2	1673	6085	9224	14,897	326,987	22.8	13.8	405	26.5	575	0.592	0.059	5.66	0.723133				
CN_10	Neoproterozoic	28.5	1385	15,404	3172	3098	284,868	18.3	7.39	870	8.01	469	0.973	0.091	3.03	0.723231	−0.583	± 0.065	203.24	± 22.97
CN_11	Neoproterozoic	20.6	158	30,750	820	1160	257,979	5.22	22.2	52.6	0.872	2019	–	0.163	1.37	0.708312				
CN_12	Neoproterozoic	29.6	289	22,890	2421	1898	342,570	5.10	20.8	33.8	1.63	3125	–	0.422	2.5	0.708376				
CN_13	Neoproterozoic	27.5	1636	22,074	3495	2213	286,473	13.9	6.77	527	5.63	698	–	0.208	9.83	0.709919	−0.448	± 0.043	75.63	± 12.40
IN_1	Paleoproterozoic	37.1	60	514	3523	1703	317,653	16.4	2.69	3436	9.14	279	0.277	0.797	3.4	0.715257	−0.363	± 0.053	12.11	± 16.93
IN_2	Paleoproterozoic	28.4	40	725	1265	858	222,920	12.0	1.28	729	4.71	166	–	0.068	1.63	0.714516				
IN_3	Paleoproterozoic	14.2	–	50,608	120	96.3	218,907	4.0	1.31	394	0.381	142	–	0.033	0.464	0.710946	−0.453	± 0.048	42.01	± 13.78
IN_4	Paleoproterozoic	37.3	33	255	1498	779	304,317	12.1	3.2	292	4.32	234	0.203	0.373	9.83	0.712921				
IN_5	Paleoproterozoic	28.2	109	536	700	598	215,223	81.7	12.5	20,325	1.68	210	2.87	1.14	11.8	0.717493				
IN_6	Paleoproterozoic	32.3	207	5018	2640	1042	302,087	25.7	5.11	4540	6.04	331	0.55	0.688	2.92	0.713232	−0.402	± 0.069	−16.83	± 13.55

concentration (53.5 to 121 mg/kg; $n = 7$) (Table 1, Fig. 2B). There are no significant variations within U concentrations throughout this period of time ($p = 0.62$), while the $\delta^{238}U$ increase with increasing age ($\rho = 0.57$, $p = 0.01$). A significant difference in the $\delta^{238}U$ and U concentration was observed between PRs deposited before the Paleozoic Oxygenation Event (~ 400 Ma) and those that are younger ($p < 0.01$) (Fig. 2). Young PR samples have $\delta^{238}U$ greater than that of modern seawater (−0.38 ‰) and, with the exception of one sample, greater than the average continental crust (−0.29 ‰) (Tissot and Dauphas, 2015).

Older PRs, includes those from China and India, have a lower and narrower range of U concentration between 0.5 and 20.6 mg/kg ($n = 19$). Among these PRs, we observed a significant higher U concentration of PRs deposited during the Phanerozoic compared to those deposited during the Proterozoic (mean of 16.1 mg/kg vs 4.5 mg/kg, $p < 0.01$). Interestingly, although the PRs of Devonian age are not as enriched in U as the younger PRs, they have $\delta^{238}U$ values within the same range as the young marine rocks (Fig. 2). The $\delta^{238}U$ for other old PR samples (Cambrian to Proterozoic; $n = 7$) vary between −0.583‰ and −0.363‰. These values, within error, are at or below $\delta^{238}U$ values of modern seawater and continental crust, as well as lower than the values of the younger PRs (Fig. 2A).

As indicated by $\delta^{234}U$ (Table 1 and Fig. 2B), not all the investigated PRs are in secular equilibrium. For young samples, deviation from secular equilibrium is not accompanied by any variation in the $\delta^{238}U$. However, the $\delta^{238}U$ values of PRs are lower in Precambrian PR samples associated with shifts in the $\delta^{234}U$ secular equilibrium (Fig. 3). The strong linear relationship of the $\delta^{234}U$ and $\delta^{238}U$ of Precambrian PRs suggests a $\delta^{238}U$ value of −0.396‰ at $\delta^{234}U$ of 0‰ ($r^2 = 0.85$, $p < 0.01$) (Fig. 3).

3.3. Strontium isotopes

$^{87}Sr/^{86}Sr$ ratios were measured in all sedimentary PRs ($n = 70$; Tables 1, S2). The $^{87}Sr/^{86}Sr$ values of younger PRs (< ~75 Ma) generally follow the secular seawater $^{87}Sr/^{86}Sr$ curve (McArthur et al., 2020; Chen et al., 2022), except for PR samples from Western Sahara, Senegal, and Togo with $^{87}Sr/^{86}Sr$ deviate from the expected secular seawater $^{87}Sr/^{86}Sr$ during time of deposition, with a range of 0.707533 to 0.708919 (Fig. 4A). Mid-Permian PRs from the Phosphoria Formation range from 0.707382 to 0.708268 (Fig. 4A). Old PRs from China and India are generally more radiogenic than expected coeval seawater (McArthur et al., 2020), with only 2 samples from China (376 and 535 Ma) having an $^{87}Sr/^{86}Sr$ value consistent with that expected of seawater during the time of deposition (Fig. 4B). The Sr isotope ratios measured in this study generally agree with previously reported values for PRs, including those from Senegal and Togo (Sattouf et al., 2007), the Tethys Mediterranean Belt (Soudry and Yaacov, 2005; Soudry et al., 2006) and the Floridian PRs (Compton et al., 1993; Mallinson et al., 1994).

The concentration of Sr in PRs varies between and within localities of PRs, ranging from 142 to 3125 mg/kg for all PRs (Table 1). PRs from India and Western Sahara have the lowest Sr concentrations with a narrow range of 142 to 331 mg/kg, followed by PRs from Togo (382–417 mg/kg), Morocco (870–1000 mg/kg), Syria (1232–1593 mg/kg), Algeria (1808–2129 mg/kg), and Tunisia (1809–2051 mg/kg). The Sr concentrations of PRs from the US, Israel, Senegal, and China are more variable between 347 and 3125 mg/kg. Generally, there is a trend of decreasing Sr concentrations in PRs with increasing age ($\rho = -0.30$, $p < 0.05$; Fig. S5), although some of the Precambrian PRs from China deviate from this trend with elevated Sr concentrations.

4. Discussion

4.1. The distribution of trace elements in phosphate rocks

During weathering, diagenesis, and metamorphism, carbonate is released from the carbonate-fluorapatite structure and is converted to

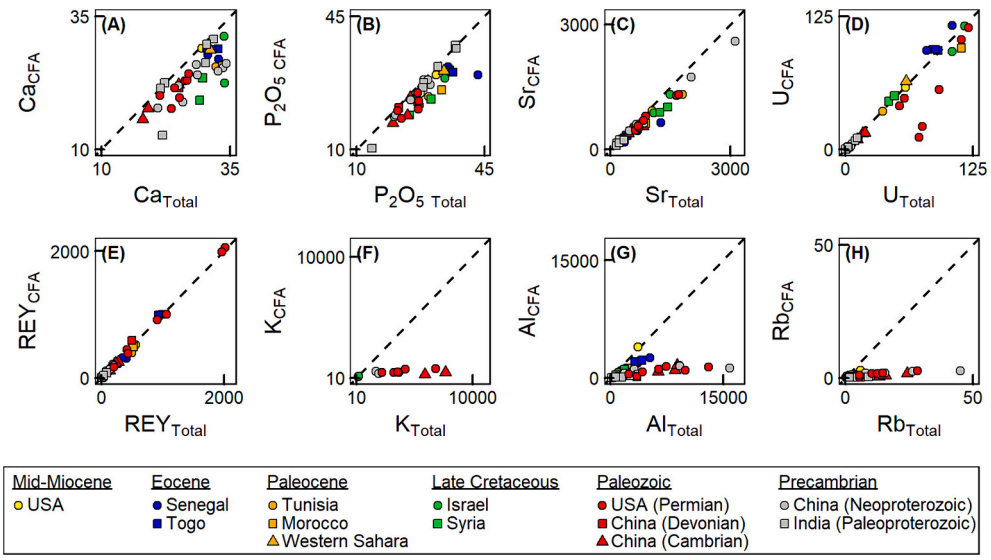

Fig. 1. Enrichment of select elements and REY in the phosphate phase (CFA phase) compared to the bulk rock (total digest). Concentration units are mg/kg, with the exception of Ca and P_2O_5 (wt%). The dashed black line represents a 1:1 concentration ratio between CFA phase and bulk rock. Potassium was not detected above the detection limit for the majority of analyzed CFA phases.

Table 2
Summary of elemental concentrations of young vs old phosphate rock, for elements that are notably enriched in younger phosphate rocks. Mid-Permian phosphate rocks are entirely derived from the Phosphoria Formation. Seven old phosphate rock samples are below limit of detection for Mo. (mean ± 1σ).

	V	Cr	Mo	Cd	U
Young Phosphate Rock (n = 44)	104 ± 63.3	139 ± 76.3	4.98 ± 3.72	23.6 ± 22.3	87.8 ± 29.7
Mid-Permian Phosphate Rock (n = 7)	112 ± 26.9 1658, 2645	563 ± 165	14.6 ± 9.65 52.3, 125	≤ 2.67 (*n* = 4) ≥ 112 (*n* = 3)	83.8 ± 26.3
Old Phosphate Rock (n = 19)	26.6 ± 23.7	23.2 ± 25.4	1.63 ± 1.97 (*n* = 12)	0.42 ± 0.40	7.72 ± 6.21

fluorapatite (Pufahl and Groat, 2017). The sequential leaching experiments we conducted show larger fractions of P_2O_5 were leached during the CFA leach step (1 M HCl) in older PRs compared to younger rocks ($p < 0.01$, Fig. S6). Complementarily, younger rocks had larger fractions of P_2O_5 leached during the carbonate leach step (1 M HOAc) ($p < 0.01$, Fig. S6). This suggests carbonate-fluorapatite is more susceptible to leaching by 1 M HOAc than fluorapatite. Nonetheless, the 1 M HCl leachate is representative of the (carbonate)-fluorapatite structure, with some influence from the co-occurring dolomite mineral (see discussion below).

Sequential leaching experiments show that the distribution of trace elements in PRs varies strongly with age. On average, 60% of Al is found in the CFA phase for young PRs ($n = 13$), while <20% of Al is found in the CFA phase of all but three PR of Mid-Permian to Precambrian PRs ($n = 25$) (Table S6). In addition to Al, significantly higher percentages of trace elements of V, Cr, Mn, Co, Cu, As, Rb, and Cd are found in the CFA phase of young PRs compared to Devonian to Precambrian PRs ($p < 0.01$, Table S6). Permian PRs are variable in these trace metal associations, though As is more associated with the CFA phase similar to younger PRs; the opposite is true for Cd.

Nearly all U found in young PRs occur within the CFA phase, but only a fraction (mean ~ 71%) of the U in Permian to Precambrian PRs occur within the CFA phase (Table S6). On average, 14% of the U in Precambrian PRs occur within the carbonate phase, while residual fractions of U in Permian rocks are assumed to be in the non-carbonate and non-CFA phases (Table S7). Consequently, the U isotope measurements were conducted after selective leaching of the CFA phase in the rocks. A variable fraction (47% - 92%) of Sr occurs within the CFA phase of the investigated PRs (Table S6, S7). Analysis of the Sr isotope composition was conducted for both the selected CFA phase and bulk PRs.

The Mg/Ca ratio can be used as an indicator of dolomite occurrence in PRs. The Mg/Ca ratios of young and Permian PRs range between 0.0004 and 0.047 (Fig. S7, Table S8). PRs for which dolomite was identified via XRD have the highest Mg/Ca (>0.01). PRs from China primarily contain an Mg/Ca range of 0.04–0.12, with the Cambrian samples and one Neoproterozoic sample having Mg/Ca below 0.02. PRs from India generally are within a similar range as young PRs, with the exception of one sample for which dolomite was identified as a major mineral and which correspondingly has Mg/Ca of 0.23. Although the Mg/Ca ratio is lower within the CFA phase (<0.007 for Miocene to Permian PRs), the Mg/Ca for that of several PRs from China (0.002–0.051) and one from India remained elevated (0.190). This higher Mg/Ca ratio suggests the dissolution of residual dolomite during the leaching of CFA from the PRs.

The Al/Ca of most PRs falls below 2.0×10^{-2}, with several Permian, Cambrian, and Neoproterozoic PRs having elevated Al/Ca up to 7.6×10^{-2} (Fig. S7, Table S8). The CFA phase shows an order of magnitude reduction in the Al/Ca when compared to the bulk ratio for most PRs of Permian to Precambrian age. The change in the Al/Ca of these PRs in the extracted CFA phase suggests that Al (an indicator of detrital material, Tribovillard et al., 2006) is not associated with the CFA phase of PRs (Fig. 1). Furthermore, the two PRs from China with the highest Al/Ca also have high quartz content (>30%) measured via XRD (Table S4).

A previous study has suggested Mn substitution for Sr in PRs during diagenesis is due to exposure to meteoric fluids (Kaufman and Knoll, 1995). Young PRs from the USA, Peru, Senegal, and Togo (Miocene to mid-Eocene, $n = 18$) have Mn/Sr between 0.1 and 1; with one USA and Peru sample having a lower Mn/Sr (0.010 and 0.036 respectively), and one sample from Senegal and Togo exceeding this range with an Mn/Sr of 1.98 and 1.06 respectively (Fig. S7, Table S8). In contrast, PRs from Algeria, Tunisia, Morocco, Israel, Syria, and Jordan (early-Eocene to Permian, $n = 31$) have lower Mn/Sr ratios between 0.001 and 0.1. Paleoproterozoic PRs from India ($n = 5$) have extremely elevated Mn/Sr between 1.25 and 13.7, with one sample containing major amounts of goethite as determined by XRD, having an Mn/Sr of 96.8. For most samples there are no differences between the Mn/Sr ratios of the bulk PR

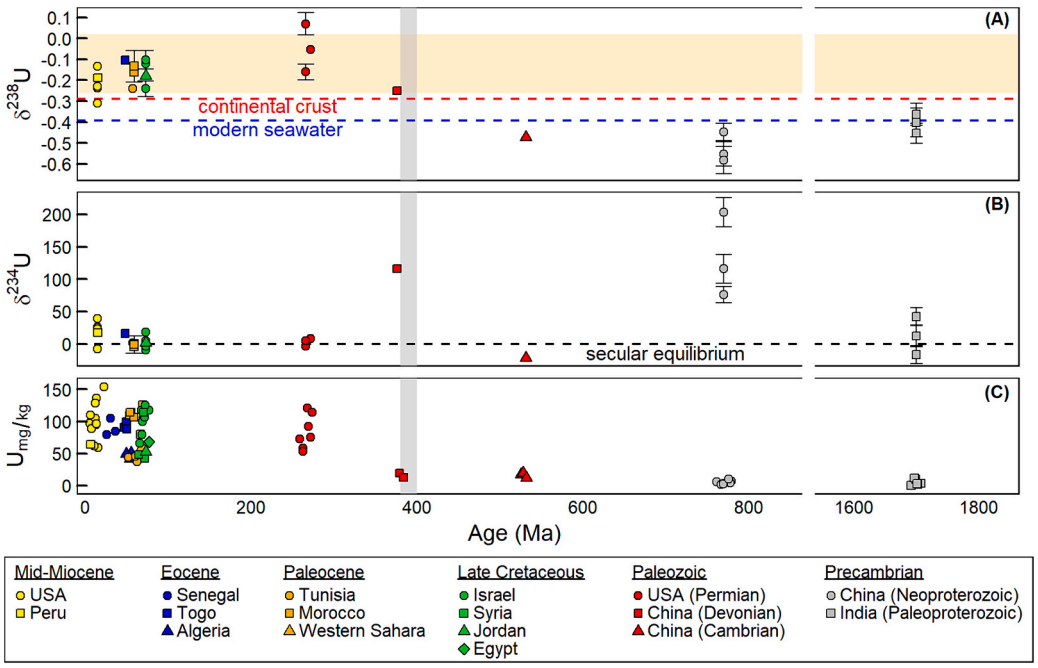

Fig. 2. (A) $\delta^{238}U$, (B) $\delta^{234}U$, and (C) U concentrations of sedimentary phosphate rocks analyzed in this study. The orange shaded region depicts the values observed in diagenetically-modified carbonate sediments ($\Delta^{238}U_{sw} \sim 0.27 \pm 0.14$) (Chen et al., 2018). The shaded gray region represents the estimated inception of the Paleozoic Oxygenation Event. Legend represents the age and location of the sedimentary phosphate rocks evaluated in this study.

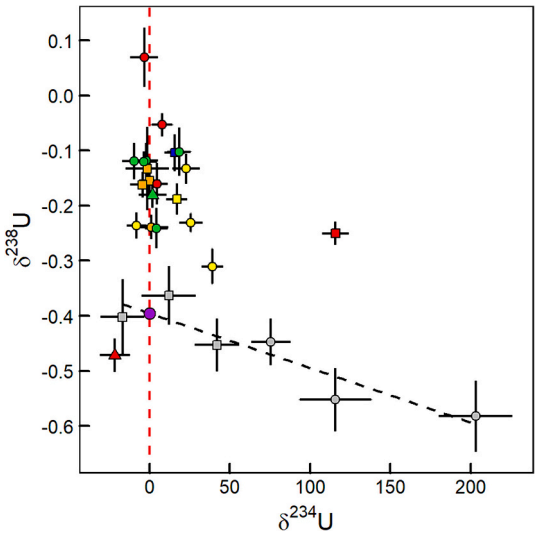

Fig. 3. The relationship between $\delta^{234}U$ and $\delta^{238}U$ of analyzed phosphate rocks. The red dashed line represents secular equilibrium. The black dashed line represents the relationship between the $\delta^{234}U$ and $\delta^{238}U$ ($r^2 = 0.85$, $p < 0.01$) of Precambrian samples to estimate the $\delta^{238}U$ value of the Precambrian phosphate rocks (−0.396‰, purple point) at $\delta^{234}U$ of 0‰. See legend for the age and location of the phosphate rocks in Fig. 2. (For interpretation of the references to colour in this figure legend, the reader is referred to the web version of this article.)

and CFA phase. Of note, the one PR from Togo exceeding an Mn/Sr of 1 in the bulk rock has a nearly identical Mn/Sr of other samples from Togo in the CFA phase (Table S8). Similarly, the Mn/Sr in the of PRs from India were lower in the CFA phase (0.1–1) than in the bulk rock (1.25–13.7), with the anomalous goethite bearing PR containing an Mn/Sr of 8.3 in the CFA phase.

High Rb/Sr can be indicative, primarily in older PRs, of incorporation of ^{87}Sr from ^{87}Rb decay. This potentially could modify the $^{87}Sr/^{86}Sr$ ratio away from the original composition. The Rb/Sr ratios of young PRs are $<1 \times 10^{-2}$, with the exception of the PR from Western Sahara, which has elevated Rb/Sr of 1.5×10^{-2} (Fig. 5A, Table S8). Rb/Sr ratios of older bulk PRs vary widely (0.04×10^{-2}–5.5×10^{-2}), with an average of 1.96×10^{-2}. Targeted analysis of the CFA phase in older PRs yielded Rb/Sr $\leq 0.52 \times 10^{-2}$, which is in the same range as young PRs. We conducted an isotope correction using the excess Rb and the age of the host geological formations to predict the possible $^{87}Sr/^{86}Sr$ alteration by ^{87}Rb decay (Bentley, 2006). Our analysis shows that only a relatively small increase in the $^{87}Sr/^{86}Sr$ is possible, up to 0.0009 or 0.0006 for Paleo- or Neoproterozoic PRs, respectively. Therefore, the $^{87}Sr/^{86}Sr$ data reported in this study do not reflect overprinting from ^{87}Rb decay.

During diagenesis, Sr, which substitutes for Ca, is removed from the crystal structure, thereby decreasing the Sr/Ca ratio of CFA (McArthur et al., 1987; Mcarthur, 1985). The Sr/Ca of most PRs fall between 2×10^{-3} to 9×10^{-3} ($n = 53$) (Fig. 5B, Table S8). Exceptions to this are all PRs from India, Western Sahara, and Togo, and one from the USA and Senegal, and five samples from China with lower Sr/Ca ratios, within a range of 0.6×10^{-3} to 2×10^{-3} ($n = 17$). We find a strong correlation between Sr and Sr/Ca in all PRs through time ($\rho = 0.96$; Fig. S5). Specifically, low Sr/Ca ratios are associated with low Sr concentrations in older PRs. A similar trend was observed for U and U/Ca ratios in PRs, which decrease through time ($\rho = 0.98$, Fig. S8). While the U/Ca of most Permian and younger PRs are $>2 \times 10^{-4}$ ($n = 33$, Fig. 5B, Table S8), the U/Ca of older PRs are $<1 \times 10^{-5}$ ($n = 19$). Those PRs from Algeria, Tunisia, Western Sahara, and Jordan have relatively lower U/Ca ratios, between 1×10^{-5} and 2×10^{-5} ($n = 8$). Our data show no significant difference in the U/Ca and Sr/Ca ratios between the CFA phase and the bulk PRs ($p > 0.05$, Fig. 5), likely due to the primary association of U and Sr with the CFA phase. Overall, these trends are consistent with progressive removal of Sr, and possibly U, from the CFA phase during diagenesis, which differentiate diagenetically modified from other young FRs. However, as will be discussed below, the secular changes in U and U/Ca are more strongly driven by the redox evolution of the ocean and depositional settings of older (i.e., Precambrian) PRs.

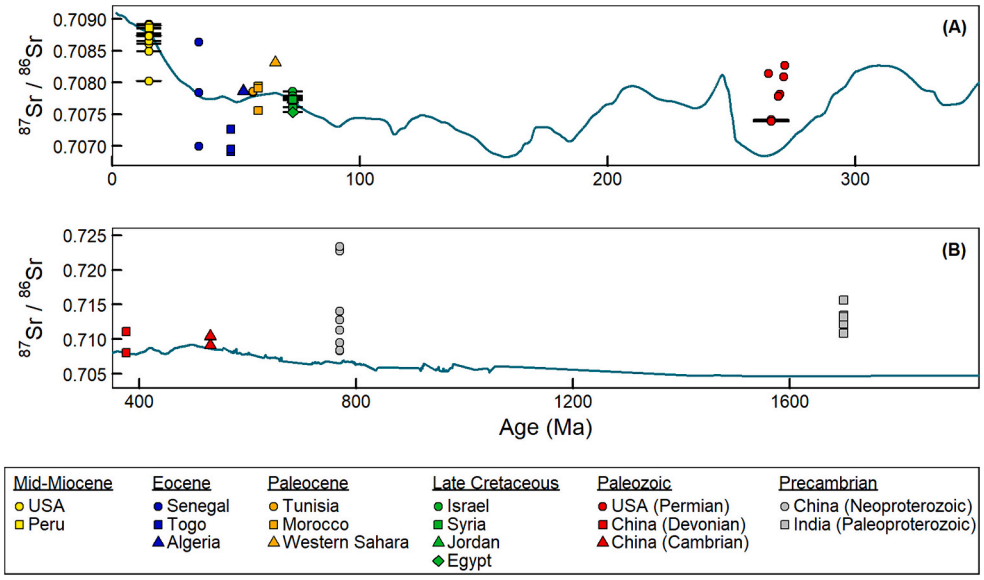

Fig. 4. $^{87}Sr/^{86}Sr$ of Mid-Miocene to Permian (A) and Devonian to Precambrian (B) PRs analyzed in this study. The blue line represents the currently accepted Phanerozoic $^{87}Sr/^{86}Sr$ of seawater (McArthur et al., 2020) and the available data for Precambrian seawater summarized by Chen et al. (2022). Due to significant and relatively rapid changes in the $^{87}Sr/^{86}Sr$ of seawater during the Miocene, Late Cretaceous, and Permian, error bars were included on data points for these geological time intervals. (For interpretation of the references to colour in this figure legend, the reader is referred to the web version of this article.)

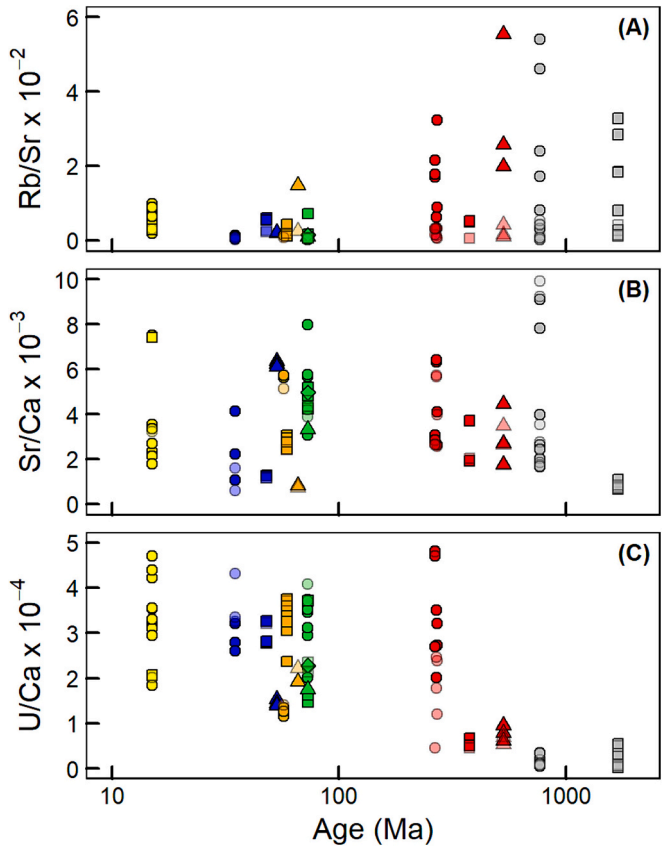

Fig. 5. Evaluation of the Rb/Sr (A), Sr/Ca (B), and U/Ca (C) in bulk phosphate rock (solid points) and phosphate phases (transparent points). See legend for the age and location of the PRs in Fig. 4.

4.2. Reconstructing paleo-redox conditions with uranium isotopes

The $\delta^{238}U$ of marine sediments can vary significantly. Primary (biogenic) carbonates precipitated directly from oxic seawater often record the isotope composition of seawater without isotope fractionation ($\Delta^{238}U \sim 0‰$). In contrast, sediments deposited under anoxic conditions are typically positively fractionated relative to seawater ($\Delta^{238}U$ up to ~0.6‰), reflecting the selective incorporation of ^{238}U into the solid phase. However, manganese crusts and nodules have lower $\delta^{238}U$ than seawater ($\Delta^{238}U \sim -0.2‰$), reflecting preferential adsorption of the lighter isotope ^{235}U (Zhang et al., 2020; Weyer et al., 2008; Chen et al., 2018; Romaniello et al., 2013; Goto et al., 2014).

The $\delta^{238}U$ values of the analyzed young PRs ($\delta^{238}U = -0.311$ to -0.102, Fig. 2A) fall within the range previously reported for modern carbonate sediments (Chen et al., 2018; Tissot et al., 2018), including the Permian PRs with $\delta^{238}U$ range of $\delta^{238}U = -0.311‰$ to $+0.070‰$. These values are more positive than modern seawater (−0.38‰, Kipp et al., 2022) and the continental crust (−0.29‰, Tissot and Dauphas, 2015), likely indicating isotope fractionation associated with U reduction in anoxic pore waters, which was retained in CFA (Chen et al., 2018; Yuan et al., 2023). The heavier $\delta^{238}U$ values observed in the young and Permian PRs provide further evidence for CFA formation in anoxic depositional environments, or at least with anoxic porewaters during early-stage diagenesis.

In contrast to younger PRs, Cambrian and Precambrian PRs have lower $\delta^{238}U$ values and lower U concentrations. The intercept value of the linear correlation between the $\delta^{234}U$ and $\delta^{238}U$ of the Precambrian samples might suggest a modeled CFA $\delta^{238}U$ value of $\sim -0.396‰$ in Precambrian PRs (Fig. 3), because lower $\delta^{238}U$ values in Neoproterozoic PRs are accompanied by high $\delta^{234}U$, indicative of recent modification of the original $\delta^{238}U$ signature (see discussion below) (Fig. 3). This modeled CFA $\delta^{238}U$ value is similar to the modern seawater value yet is lower than that of the least altered younger PR samples (Fig. 2A).

Studies of modern to Mesozoic phosphates suggest that, in sediment porewaters, the removal of ^{238}U via reduction and addition of ^{234}U via alpha recoil from surrounding sediments may drive the coupled evolution of $\delta^{234}U$ and $\delta^{238}U$ in porewaters as they age (Kolodny et al., 2017; Li et al., 2024). If such porewaters are subjected to more reducing conditions, authigenic enrichment of uranium can occur, thereby recording very high $\delta^{234}U$ (e.g., Redmond et al., 2023) and low $\delta^{238}U$. While this mechanism can drive $\delta^{234}U$ and $\delta^{238}U$ covariation such as that observed here, the short half-life of ^{234}U (245 kyr) relative to the age of the PRs (Myr to Gyr) requires that such a process must have

operated during recent alteration of these samples (at least for the $\delta^{234}U$ signatures). Furthermore, Kolodny et al. (2017) observed lower $\delta^{238}U$ and higher $\delta^{234}U$ values in the U(VI) fraction of phosphorites compared to the bulk or the U(IV) fraction. The coupled process of U reduction and alpha recoil could suggest the $\delta^{238}U$ of Precambrian PRs, in tandem with low U concentrations, may be representative of the authigenic enrichment of aged porewaters.

One might instead suggest that the $\delta^{238}U$ difference between young and old PRs stems from a primary difference in $\delta^{238}U_{sw}$ over geological time, driven by a change in the extent of seafloor anoxia. Several studies have suggested that more pervasive ocean anoxia during the Precambrian resulted in a more negative seawater $\delta^{238}U$ value, with a completely anoxic ocean having a $\delta^{238}U$ as low as −0.9‰ (Kipp and Tissot, 2022; Chen et al., 2021; Gilleaudeau et al., 2019). We hypothesize that the low U content coupled with low $\delta^{238}U$ values reflect expansive deep ocean water anoxia during these depositional periods, and consequently, immobility of U in reduced waters that led to a lower magnitude of U uptake into CFA from low-U pore water in the diagenetic zone. This is supported by a similar trend of low U content and low $\delta^{238}U$ values in Precambrian carbonates (Gilleaudeau et al., 2019; Chen et al., 2021).

4.3. Comparison of strontium isotope ratios in phosphate rocks to the secular seawater curve

Unlike the $\delta^{238}U$, the $^{87}Sr/^{86}Sr$ isotope ratio does not fractionate during the incorporation of Sr into CFA from pore water. As such, it is expected that the $^{87}Sr/^{86}Sr$ of the original PRs would mimic the composition of contemporaneous seawater that infiltrated the early diagenetic environment of CFA deposition. This has been demonstrated by systematically similar Sr isotope ratios of modern phosphate rock deposits to that of both modern seawater and the and marine pore waters in the diagenetic environment where CFA is generated (Kolodny and Luz, 1992).

The Sr isotope variations of young PRs presented in this study generally follow the secular $^{87}Sr/^{86}Sr$ seawater curve (McArthur et al., 2020), with a few exceptions. However, outside of one Cambrian and one Devonian PR sample with $^{87}Sr/^{86}Sr$ ratios consistent with the seawater Sr isotope curve, older PRs are substantially more radiogenic than contemporaneous seawater, which is based on the $^{87}Sr/^{86}Sr$ of marine carbonates from the same ages (Chen et al., 2022). Our sequential leaching experiments reveal that the $^{87}Sr/^{86}Sr$ ratios of the CFA phase are only generally slightly lower (i.e., less radiogenic) than the $^{87}Sr/^{86}Sr$ of the bulk PRs (Fig. 6), indicating that the $^{87}Sr/^{86}Sr$ variations and deviation from the seawater curve detected in the bulk PRs generally represents the CFA phase of these PRs.

Data from Eocene PRs from Senegal ($n = 3$) show higher and lower $^{87}Sr/^{86}Sr$ ratios relative to the contemporaneous seawater, in which higher Sr concentration are associated with lower $^{87}Sr/^{86}Sr$ (Table 1). Similarly, the $^{87}Sr/^{86}Sr$ ratios of PRs from Togo (Eocene) and Western Sahara (Paleocene) deviate from contemporaneous seawater (Fig. 4). Previous studies have shown that the low Sr/Ca ratios in the CFA phases of PRs can be used to indicate late diagenetic modification of the original composition of PRs because less Sr may be incorporated into diagenetically-modified CFA (McArthur et al., 1987). The Sr/Ca ratios of the CFA phase of PRs from Togo, Senegal, and Western Sahara are consistently the lowest among the investigated young PRs (Fig. 7). These samples also have lower Na and Mg concentrations in the CFA phase than other young PRs (Fig. 7), further possible indications of diagenetic modification (Mcarthur, 1985).

There is no significant change in the Sr/Ca ratios of PRs through geological time (Fig. 5B, $p > 0.05$). An examination of the Sr/Ca of PRs within geologic time periods provides insight into potential modification of $^{87}Sr/^{86}Sr$ in the CFA phase of old PRs. While Paleoproterozoic PRs from India have very low Sr/Ca < 1 [10^{-3}] (Fig. 5B) and are more radiogenic than contemporaneous seawater, we recognize three distinct

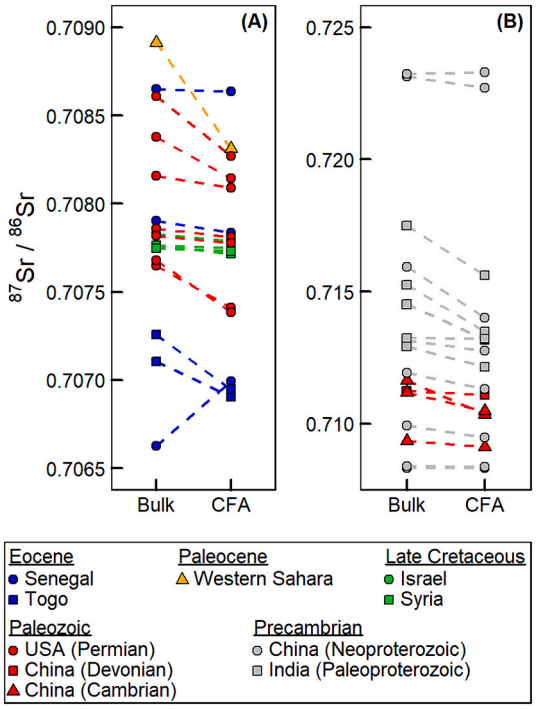

Fig. 6. Comparison of the $^{87}Sr/^{86}Sr$ of bulk phosphate rock (Bulk) and selectively extracted phosphate phase (CFA) conducted through sequential leaching experiments. Data is represented in (A) young and Permian phosphate rocks and (B) old phosphate rocks.

groups of Sr/Ca and $^{87}Sr/^{86}Sr$ in the CFA phases of Neoproterozoic PRs from China: (1) low Sr/Ca with high $^{87}Sr/^{86}Sr$ ($n = 2$); (2) high Sr/Ca with relatively low $^{87}Sr/^{86}Sr$ (n = 2); and (3) moderate Sr/Ca and $^{87}Sr/^{86}Sr$ ($n = 4$) (Fig. 8). The Devonian (n = 2) and Cambrian (n = 3) PRs generally follow the same trend, for which the highest Sr/Ca is observed in the lowest $^{87}Sr/^{86}Sr$. In the case of these older PR, lower $^{87}Sr/^{86}Sr$ is more characteristic of contemporaneous seawater, and therefore samples with low $^{87}Sr/^{86}Sr$ and high Sr/Ca ratios would represent the least diagenetically modified PRs from China.

5. Integration: changes in seawater composition versus diagenetic modification

Our data show that both the U and Sr isotope compositions of marine Paleozoic and Precambrian PRs are distinct from those of Miocene to Late Cretaceous PRs. Changes in the U isotope compositions are most likely a result of changes in seawater composition. We posit that Precambrian U-depleted suboxic to anoxic bottom seawater infiltrated the diagenetic environment of CFA deposition, resulting in lower $\delta^{238}U$ values relative to the composition of younger PRs. In contrast, it has been argued that low U in older PRs rather reflect diagenetic alteration of the original composition of the PRs (Sun et al., 2020). One clue for such later modification is the deviation of $\delta^{234}U$ from secular equilibrium, indicating recent alteration. The systematic relationship between $\delta^{238}U$ and $\delta^{234}U$ (Fig. 3) suggests that the U system in some of these PRs was perturbed during the past 200 kyr, and therefore the original $\delta^{238}U$ composition could be masked by recent reactions with terrestrial water of low $\delta^{238}U$ fluids (though such isotopic compositions are not common). However, other PRs such as the Early Cambrian from China ($n = 1$) and Paleoproterozoic from India (n = 2) have low $\delta^{238}U$ and yet their $\delta^{234}U$ values are at secular equilibrium (Fig. 3), similar to those of many young PRs. We therefore infer that recent modification of $\delta^{238}U$ in CFA might have occurred to some extent, but it cannot wholly explain the difference between the $\delta^{238}U$ of Precambrian and younger PRs. Although the $\delta^{234}U$ cannot explain possible modification beyond the

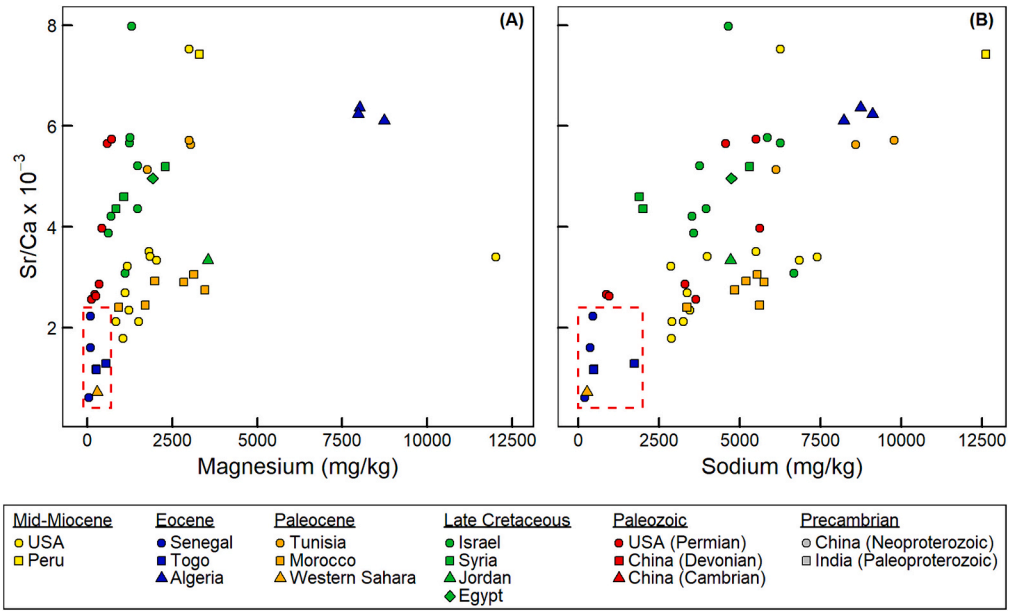

Fig. 7. Comparison of the (A) Mg and (B) Na to the Sr/Ca content of the CFA phases of young and Permian phosphate rocks. CFA phases of phosphate rocks from Western Sahara, Togo, and Senegal (red dashed box) have low Sr/Ca, Mg, and Na which combined can be indicative of diagenetic modification (Mcarthur, 1985). (For interpretation of the references to colour in this figure legend, the reader is referred to the web version of this article.)

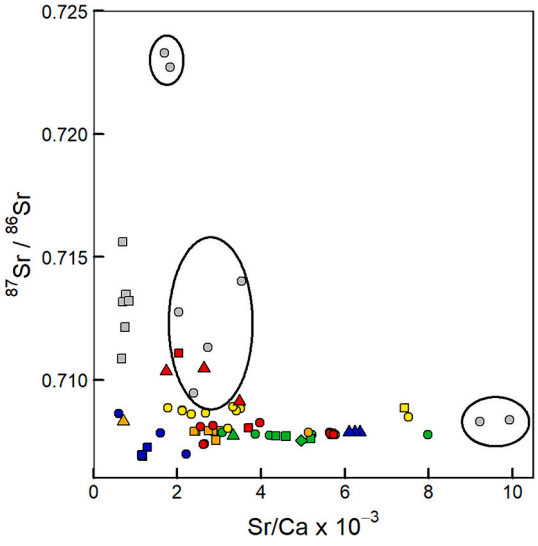

Fig. 8. Relationship between the Sr/Ca ratio and the ^{87}Sr/^{86}Sr of phosphate rocks. The black ellipses indicate three distinct groups within the Neoproterozoic phosphate rocks from China (gray circles): low Sr/Ca with high ^{87}Sr/^{86}Sr, (2) high Sr/Ca with relatively low ^{87}Sr/^{86}Sr, and (3) moderate Sr/Ca and ^{87}Sr/^{86}Sr.

past 200 kyr, the difference between the groups likely derives from the redox evolution of seawater as recorded by the δ^{238}U variations in carbonate sediments (Chen et al., 2021). Furthermore, the shift in the δ^{238}U of PRs to values higher than modern seawater during the Paleozoic supports a Paleozoic Oxygenation Event driving ocean redox to modern conditions around ~400 Ma, which has been supported by modeling and other ocean redox indicators such as I/Ca ratios, Ce anomalies, and δ^{98}Mo in carbonates (Elrick et al., 2022; Lenton et al., 2016; Lu et al., 2018; Sperling et al., 2015; Wallace et al., 2017).

We interpret the ^{87}Sr/^{86}Sr variations to reflect either changes in (i) depositional environment of CFA formation, (ii) diagenetic modification, or (iii) a combination of both. In Miocene to Late Cretaceous PRs, Sr/Ca trends show clear evidence of diagenetic modification altering the original ^{87}Sr/^{86}Sr ratio of PRs that do not follow the secular seawater curve. In Permian to Precambrian PRs, we explore two different possible scenarios. The first scenario is that late diagenetic modification and re-equilibrium of the Permian to Precambrian PRs with non-marine fluids with terrestrial (radiogenic) ^{87}Sr/^{86}Sr resulted in modification of the ^{87}Sr/^{86}Sr of old PRs. Deeper burial may also cause a greater extent of alteration of the ^{87}Sr/^{86}Sr due to the exchange of Sr between CFA and pore fluids (Richter and DePaolo, 1987; Voigt et al., 2015). Previous studies have suggested that Sr/Ca can be used as an indicator for late diagenetic modification (McArthur et al., 1987; Mcarthur, 1985). In examining all PRs in this study, a Sr/Ca > 0.002 is observed in PRs that mostly resemble original marine conditions, and therefore lower Sr/Ca ratios can be an indicator of late diagenetic modification of ^{87}Sr/^{86}Sr. For younger PRs, we clearly see that low Sr/Ca ratios are associated with different ^{87}Sr/^{86}Sr ratios relative to the expected secular seawater Sr isotope composition for certain PRs from Western Sahara, Togo, and Senegal (Fig. 8). Yet, for the Precambrian PRs we see mixed patterns; in some Neoproterozoic PRs from China, low Sr/Ca ratios are associated with high ^{87}Sr/^{86}Sr that could reflect diagenetic modification, while others have moderate to high Sr/Ca but are still associated with high ^{87}Sr/^{86}Sr, above that of Precambrian seawater (Fig. 8). In contrast, the Sr/Ca of the Paleoproterozoic PRs from India have systematically lower Sr/Ca ratios that are associated with highly radiogenic ^{87}Sr/^{86}Sr that may be a result of later diagenetic alteration.

A second, more likely, scenario is the contribution of terrigenous materials, containing radiogenic ^{87}Sr/^{86}Sr, to the local depositional environment of CFA formation resulting in high ^{87}Sr/^{86}Sr in Precambrian PRs. Precambrian PR formation may have occurred in local oxygen oases in peritidal environments (Drummond et al., 2015). The peritidal nature of these deposits allows for the integration of more radiogenic ^{87}Sr/^{86}Sr from terrigenous material in a zone of heterogeneity with respect to the open ocean ^{87}Sr/^{86}Sr composition. This scenario is consistent with the non-marine like REY distribution patterns observed in the Precambrian PRs (detected from the same sample collection) along with less radiogenic Pb isotope compositions likely indicating a terrigenous contribution measured in the same PR sample collection (Wang et al., 2023). The inclusion of quartz in many Precambrian PRs (Table S4) is further evidence of detrital terrigenous materials. In this

scenario, both the radiogenic $^{87}Sr/^{86}Sr$ and low $\delta^{238}U$ of Precambrian PRs could reflect geochemical overprinting of terrigenous inputs to the original depositional environment of PR formation.

Another version of this "enhanced terrigenous input" explanation for the deviation of the $^{87}Sr/^{86}Sr$ ratios in PRs from contemporaneous seawater, is deposition of the PRs in highly restricted basins isolated from the open ocean. This is exhibited by the Permian PRs originating from the Phosphoria Formation, in which a highly restricted basin environment has been suggested due to the abundance of evaporite deposits surrounding the basin (Perkins et al., 2003). The basin may have received radiogenic $^{87}Sr/^{86}Sr$ input from continental runoff relative to the contribution of open seawater. Consequently, the assumption that the $^{87}Sr/^{86}Sr$ and $\delta^{238}U$ values in sedimentary PRs record the composition of contemporaneous open ocean water may not be correct due to restricted and/or isolated basins of phosphate formations.

6. Conclusions

This study presents new information on trace metal distribution, Sr isotopes ($^{87}Sr/^{86}Sr$), and radiogenic ($\delta^{234}U$) and stable ($\delta^{238}U$) U isotopes of phosphate rocks (PRs) ranging from Miocene to Paleoproterozoic in age. Through sequential leaching procedures, we found higher concentrations of Al, V, Cr, Cd, and U in young (i.e., Miocene to Late Cretaceous) relative to older (i.e., Devonian to Precambrian) PRs. In addition, we found higher percentages of these elements, in addition to Mn, Co, Cu, As, and Rb in the carbonate fluorapatite (CFA) phase, relative to the bulk PR in young PRs. The Sr isotope ratios of young PRs generally follow the secular $^{87}Sr/^{86}Sr$ seawater curve with a few exceptions that are characterized by low Sr/Ca and Na and Mg concentrations, indicative of post depositional diagenetic alterations. The $^{87}Sr/^{86}Sr$ ratios of Permian to Precambrian PRs do not follow the secular seawater curve, either due to conditions of CFA deposition (i.e., restricted basin or peritidal environment) or due to later diagenetic modification. The $\delta^{238}U$ values of young PRs are higher than that of seawater, showing preferential ^{238}U integration into CFA, characteristic of reduction of U from infiltrating seawater and retention into CFA, similar to what is commonly observed in carbonate sediments deposited under reducing porewater conditions. The $\delta^{238}U$ of older PRs are at or below the composition of modern seawater and contain much less U, indicative of deposition in a more anoxic ocean and/or reflective of diagenetic modification. In summary, the U and Sr isotopes of PRs indicate a transition in ocean redox towards a modern oxic ocean and a shift in depositional conditions of PRs during the Paleozoic, but must be carefully screened to recover signals from diagenetically-modified mineral phases.

CRediT authorship contribution statement

Robert C. Hill: Writing – review & editing, Writing – original draft, Methodology, Investigation, Data curation. **Zhen Wang:** Writing – review & editing, Methodology, Investigation, Data curation. **Gordon D.Z. Williams:** Writing – review & editing, Methodology, Investigation. **Victor Polyak:** Writing – review & editing, Validation, Methodology, Investigation, Formal analysis. **Anjali Singh:** Writing – review & editing, Investigation. **Michael A. Kipp:** Writing – review & editing, Methodology, Investigation. **Yemane Asmerom:** Writing – review & editing, Validation, Supervision, Methodology, Investigation. **Avner Vengosh:** Writing – review & editing, Writing – original draft, Validation, Supervision, Project administration, Methodology, Investigation, Funding acquisition, Data curation, Conceptualization.

Declaration of competing interest

The authors declare that they have no known competing financial interests or personal relationships that could have appeared to influence the work reported in this paper.

Data availability

The data is presented in the paper

Acknowledgement

This study was supported by NSF funded project "*From Global to Local: Geochemistry of Global Phosphate Ores and Implications for Tracing the Environmental Impacts of Fertilizers Utilization*" (EAR- 2305946). We sincerely appreciate and thank E. Schnug, R. Bol, Y. Sun, M. Abu-Hashim, T. El-Hasan, S. Haneklaus, and A. Shrivastava for their collegiality in sharing phosphate rock samples with us. We thank the two anonymous reviewers for their critical comments that have improved the clarity of this paper.

Appendix A. Supplementary data

Supplementary data to this article can be found online at https://doi.org/10.1016/j.chemgeo.2024.122214.

References

Altschuler, Z.S., 1980. The Geochemistry Of Trace elements in marine phosphorites part I. Characteristic abundances and enrichment*. In: Bentor, Y.K. (Ed.), Marine Phosphorites—Geochemistry, Occurrence, Genesis. SEPM Society for Sedimentary Geology. https://doi.org/10.2110/pec.80.29.0019.

Altschuler, Z.S., Clarke, R.S., Young, E.J., 1958. Geochemistry of Uranium in Apatite and Phosphorite (Geological Survey Professional Paper no. 314- D), Shorter Contributions to General Geology. U.S. Department of the Interior.

Bartlett, R., Elrick, M., Wheeley, J.R., Polyak, V., Desrochers, A., Asmerom, Y., 2018. Abrupt global-ocean anoxia during the late Ordovician–early Silurian detected using uranium isotopes of marine carbonates. Proc. Natl. Acad. Sci. 115, 5896–5901. https://doi.org/10.1073/pnas.1802438115.

Baturin, G.N., Kochenov, A.V., 2001. Uranium in phosphorites. Lithol. Miner. Resour. 36, 303–321. https://doi.org/10.1023/A:1010406103447.

Bentley, R.A., 2006. Strontium isotopes from the earth to the archaeological skeleton: a review. J. Archaeol. Method Theory 13, 135–187.

Chen, X., Romaniello, S.J., Herrmann, A.D., Hardisty, D., Gill, B.C., Anbar, A.D., 2018. Diagenetic effects on uranium isotope fractionation in carbonate sediments from the Bahamas. Geochim. Cosmochim. Acta 237, 294–311. https://doi.org/10.1016/j.gca.2018.06.026.

Chen, X., Tissot, F.L.H., Jansen, M.F., Bekker, A., Liu, C.X., Nie, N.X., Halverson, G.P., Veizer, J., Dauphas, N., 2021. The uranium isotopic record of shales and carbonates through geologic time. Geochim. Cosmochim. Acta 300, 164–191. https://doi.org/10.1016/j.gca.2021.01.040.

Chen, X., Zhou, Y., Shields, G.A., 2022. Progress towards an improved Precambrian seawater 87Sr/86Sr curve. Earth Sci. Rev. 224, 103869 https://doi.org/10.1016/j.earscirev.2021.103869.

Cheng, H., Lawrence Edwards, R., Shen, C.-C., Polyak, V.J., Asmerom, Y., Woodhead, J., Hellstrom, J., Wang, Y., Kong, X., Spötl, C., Wang, X., Calvin Alexander, E., 2013. Improvements in 230Th dating, 230Th and 234U half-life values, and U–Th isotopic measurements by multi-collector inductively coupled plasma mass spectrometry. Earth Planet. Sci. Lett. 371–372, 82–91. https://doi.org/10.1016/j.epsl.2013.04.006.

Chernoff, C.B., Orris, G.J., 2002. Data Set of World Phosphate Mines, Deposits, and Occurrences: Part A. Geologic Data. Part B. Location and Mineral Economic Data (USGS Numbered Series no. 2002–156), Data Set of World Phosphate Mines, Deposits, and Occurrences: Part A. Geologic Data. Part B. Location and Mineral Economic Data, Open-File Report. U.S. Geological Survey. doi: https://doi.org/10.3133/ofr02156.

Compton, J.S., Hodell, D.A., Garrido, J.R., Mallinson, D.J., 1993. Origin and age of phosphorite from the south-Central Florida platform: relation of phosphogenesis to sea-level fluctuations and δ13C excursions. Geochim. Cosmochim. Acta 57, 131–146. https://doi.org/10.1016/0016-7037(93)90474-B.

Drummond, J.B.R., Pufahl, P.K., Porto, C.G., Carvalho, M., 2015. Neoproterozoic peritidal phosphorite from the Sete Lagoas Formation (Brazil) and the Precambrian phosphorus cycle. Sedimentology 62, 1978–2008. https://doi.org/10.1111/sed.12214.

Elrick, M., Gilleaudeau, G.J., Romaniello, S.J., Algeo, T.J., Morford, J.L., Sabbatino, M., Goepfert, T.J., Cleal, C., Cascales-Miñana, B., Chernyavskiy, P., 2022. Major Early-Middle Devonian oceanic oxygenation linked to early land plant evolution detected using high-resolution U isotopes of marine limestones. Earth Planet. Sci. Lett. 581, 117410 https://doi.org/10.1016/j.epsl.2022.117410.

Filippelli, G.M., 2011. Phosphate rock formation and marine phosphorus geochemistry: the deep time perspective. Chemosphere 84, 759–766. https://doi.org/10.1016/j.chemosphere.2011.02.019.

Gabriel, S., Baschwitz, A., Mathonnière, G., Eleouet, T., Fizaine, F., 2013. A critical assessment of global uranium resources, including uranium in phosphate rocks, and

the possible impact of uranium shortages on nuclear power fleets. Ann. Nucl. Energy 58, 213–220. https://doi.org/10.1016/j.anucene.2013.03.010.
Gilleaudeau, G.J., Romaniello, S.J., Luo, G., Kaufman, A.J., Zhang, F., Klaebe, R.M., Kah, L.C., Azmy, K., Bartley, J.K., Zheng, W., Knoll, A.H., Anbar, A.D., 2019. Uranium isotope evidence for limited euxinia in mid-Proterozoic oceans. Earth Planet. Sci. Lett. 521, 150–157.
Goto, K.T., Anbar, A.D., Gordon, G.W., Romaniello, S.J., Shimoda, G., Takaya, Y., Tokumaru, A., Nozaki, T., Suzuki, K., Machida, S., Hanyu, T., Usui, A., 2014. Uranium isotope systematics of ferromanganese crusts in the Pacific Ocean: implications for the marine 238U/235U isotope system. Geochim. Cosmochim. Acta 146, 43–58. https://doi.org/10.1016/j.gca.2014.10.003.
Gupta, S.K., Chen, K.Y., 1975. Partitioning of trace metals in selective chemical fractions of nearshore sediments. Environ. Lett. 10, 129–158. https://doi.org/10.1080/00139307509435816.
Hass, A., Fine, P., 2010. Sequential selective extraction procedures for the study of heavy metals in soils, sediments, and waste materials—a critical review. Crit. Rev. Environ. Sci. Technol. 40, 365–399. https://doi.org/10.1080/10643380802377992.
Kaufman, A.J., Knoll, A.H., 1995. Neoproterozoic variations in the C-isotopic composition of seawater: stratigraphic and biogeochemical implications. Precambr. Res. Neoproter. Stratigr. Earth Hist. 73, 27–49. https://doi.org/10.1016/0301-9268(94)00070-8.
Kipp, M.A., Stueken, E.E., 2017. Biomass recycling and Earth's early phosphorus cycle. Sci. Adv. 3, eaao4795.
Kipp, M.A., Tissot, F.L.H., 2022. Inverse methods for consistent quantification of seafloor anoxia using uranium isotope data from marine sediments. Earth Planet. Sci. Lett. 577, 117240 https://doi.org/10.1016/j.epsl.2021.117240.
Kipp, M.A., Li, H., Ellwood, M.J., John, S.G., Middag, R., Adkins, J.F., Tissot, F.L.H., 2022. 238U, 235U and 234U in seawater and deep-sea corals: a high-precision reappraisal. Geochim. Cosmochim. Acta 336, 231–248. https://doi.org/10.1016/j.gca.2022.09.018.
Kolodny, Y., Luz, B., 1992. Isotope signatures in phosphate deposits: formation and diagenetic history. In: Clauer, N., Chaudhuri, S. (Eds.), Isotopic Signatures and Sedimentary Records, Lecture Notes in Earth Sciences. Springer, Berlin, Heidelberg, pp. 69–121. https://doi.org/10.1007/BFb0009862.
Kolodny, Y., Torfstein, A., Weiss-Sarusi, K., Zakon, Y., Halicz, L., 2017. 238U-235U-234U fractionation between tetravalent and hexavalent uranium in seafloor phosphorites. Chem. Geol. 451, 1–8. https://doi.org/10.1016/j.chemgeo.2016.12.032.
Lenton, T.M., Dahl, T.W., Daines, S.J., Mills, B.J.W., Ozaki, K., Saltzman, M.R., Porada, P., 2016. Earliest land plants created modern levels of atmospheric oxygen. Proc. Natl. Acad. Sci. 113, 9704–9709. https://doi.org/10.1073/pnas.1604787113.
Li, H., Kipp, M.A., Kim, S.L., Kast, E.R., Eberle, J.J., Tissot, F.L.H., 2024. Exploring uranium isotopes in shark teeth as a paleo-redox proxy. Geochim. Cosmochim. Acta 365, 158–173. https://doi.org/10.1016/j.gca.2023.11.034.
Lu, W., Ridgwell, A., Thomas, E., Hardisty, D.S., Luo, G., Algeo, T.J., Saltzman, M.R., Gill, B.C., Shen, Y., Ling, H.-F., Edwards, C.T., Whalen, M.T., Zhou, X., Gutchess, K. M., Jin, L., Rickaby, R.E.M., Jenkyns, H.C., Lyons, T.W., Lenton, T.M., Kump, L.R., Lu, Z., 2018. Late inception of a resiliently oxygenated upper ocean. Science 361, 174–177. https://doi.org/10.1126/science.aar5372.
Mallinson, D.J., Compton, J.S., Snyder, S.W., Hodell, D.A., 1994. Strontium isotopes and miocene sequence stratigraphy across the Northeast Florida Platform. J. Sediment. Res. 64, 392–407. https://doi.org/10.1306/D4267FD2-2B26-11D7-8648000102C1865D.
Mcarthur, J.M., 1985. Francolite geochemistry—compositional controls during formation, diagenesis, metamorphism and weathering. Geochim. Cosmochim. Acta 49, 23–35. https://doi.org/10.1016/0016-7037(85)90188-7.
McArthur, J.M., Hamilton, P.J., Greensmith, J.T., Boyce, A.J., Fallick, A.E., Birch, G., Walsh, J.N., Benmore, R.A., Coleman, M.L., 1987. Phosphorite geochemistry: isotopic evidence for meteoric alteration of francolite on a local scale. Chem. Geol. 65, 415–425. https://doi.org/10.1016/0168-9622(87)90017-0.
McArthur, J.M., Sahami, A.R., Thirlwall, M., Hamilton, P.J., Osborn, A.O., 1990. Dating phosphogenesis with strontium isotopes. Geochim. Cosmochim. Acta 54, 1343–1351. https://doi.org/10.1016/0016-7037(90)90159-I.
McArthur, J.M., Howarth, R.J., Shields, G.A., Zhou, Y., 2020. Chapter 7 - Strontium isotope stratigraphy. In: Gradstein, F.M., Ogg, J.G., Schmitz, M.D., Ogg, G.M. (Eds.), Geologic Time Scale 2020. Elsevier, pp. 211–238. https://doi.org/10.1016/B978-0-12-824360-2.00007-3.
Papineau, D., 2010. Global biogeochemical changes at both ends of the proterozoic: insights from phosphorites. Astrobiology 10, 165–181. https://doi.org/10.1089/ast.2009.0360.
Perkins, R., Mcintyre, B., Hein, J., Piper, D.Z., 2003. Geochemistry of Permian Rocks From the Margins of the Phosphoria Basin: Lakeridge Core. Western Wyoming.
Polyak, V.J., Curry, B.H., Lavery, D.J., Strasberg, Z.L., Cutler, S., Song, W., Crossey, L.J., Karlstrom, K.E., Asmerom, Y., 2023. Large negative δ238U anomalies in endogenic-type travertine systems. Geology. https://doi.org/10.1130/G51333.1.
Pufahl, P.K., Groat, L.A., 2017. Sedimentary and igneous phosphate deposits: formation and exploration: an invited paper. Econ. Geol. 112, 483–516. https://doi.org/10.2113/econgeo.112.3.483.
R Core Team, 2023. R: A Language and Environment for Statistical Computing.
Redmond, N.A., Hayes, C.T., Glasscock, S.K., Rohde, E., Anderson, R.F., McGee, D., 2023. Anomalous 234U/238U isotopic composition in Southern Ocean sediments. Geochim. Cosmochim. Acta 363, 40–50. https://doi.org/10.1016/j.gca.2023.09.015.
Richter, F.M., DePaolo, D.J., 1987. Numerical models for diagenesis and the neogene Sr isotopic evolution of seawater from DSDP Site 590B. Earth Planet. Sci. Lett. 83, 27–38. https://doi.org/10.1016/0012-821X(87)90048-3.
Richter, S., Eykens, R., Kühn, H., Aregbe, Y., Verbruggen, A., Weyer, S., 2010. New average values for the n(238U)/n(235U) isotope ratios of natural uranium standards. Int. J. Mass Spectrom. 295, 94–97. https://doi.org/10.1016/j.ijms.2010.06.004.
Rolison, J.M., Stirling, C.H., Middag, R., Rijkenberg, M.J.A., 2017. Uranium stable isotope fractionation in the Black Sea: modern calibration of the 238U/235U paleo-redox proxy. Geochim. Cosmochim. Acta 203, 69–88. https://doi.org/10.1016/j.gca.2016.12.014.
Romaniello, S.J., Herrmann, A.D., Anbar, A.D., 2013. Uranium concentrations and 238U/235U isotope ratios in modern carbonates from the Bahamas: assessing a novel paleoredox proxy. Chem. Geol. 362, 305–316. https://doi.org/10.1016/j.chemgeo.2013.10.002.
Sattouf, M., Kratz, S., Diemer, K., Rienitz, O., Fleckenstein, J., Schiel, D., Schnug, E., 2007. Identifying the Origin of Rock Phosphates and Phosphorus Fertilizers Through High-Precision Measurement of the Strontium Isotopes 87Sr and 86Sr. Landbauforschung Völkenrode.
Sattouf, M., Kratz, S., Diemer, K., Fleckenstein, J., Rienitz, O., Schnug, E., 2008. Significance of Uranium and Strontium Isotope Ratios for Retracing the Fate of Uranium During the Processing of Phosphate Fertilizers From Rock Phosphates, pp. 191–202.
Schulz, H.N., Schulz, H.D., 2005. Large sulfur bacteria and the formation of phosphorite. Science 307, 416–418. https://doi.org/10.1126/science.1103096.
Soudry, D., Yaacov, N., 2005. Phosphorus accumulation rates in the Upper cretaceous - Eocene of the southern Tethyan margin - a case study of temporal fluctuations in phosphogenesis and rates of phosphate fluxes. [WWW Document]. URL https://www.gov.il/BlobFolder/reports/soudri-et-al-report-2005/en/report_2005_GSI-01-2005.pdf (accessed 5.23.23).
Soudry, D., Glenn, C.R., Nathan, Y., Segal, I., VonderHaar, D., 2006. Evolution of tethyan phosphogenesis along the northern edges of the Arabian–African shield during the Cretaceous–Eocene as deduced from temporal variations of Ca and Nd isotopes and rates of P accumulation. Earth Sci. Rev. 78, 27–57. https://doi.org/10.1016/j.earscirev.2006.03.005.
Sperling, E.A., Wolock, C.J., Morgan, A.S., Gill, B.C., Kunzmann, M., Halverson, G.P., Macdonald, F.A., Knoll, A.H., Johnston, D.T., 2015. Statistical analysis of iron geochemical data suggests limited late proterozoic oxygenation. Nature 523, 451–454. https://doi.org/10.1038/nature14589.
Stewart, B.W., Chapman, E.C., Capo, R.C., Johnson, J.D., Graney, J.R., Kirby, C.S., Schroeder, K.T., 2015. Origin of brines, salts and carbonate from shales of the marcellus formation: evidence from geochemical and Sr isotope study of sequentially extracted fluids. Appl. Geochem. 60, 78–88. https://doi.org/10.1016/j.apgeochem.2015.01.004.
Stirling, C.H., Andersen, M.B., Potter, E.-K., Halliday, A.N., 2007. Low-temperature isotopic fractionation of uranium. Earth Planet. Sci. Lett. 264, 208–225. https://doi.org/10.1016/j.epsl.2007.09.019.
Sun, Y., Amelung, W., Wu, B., Haneklaus, S., Maekawa, M., Lücke, A., Schnug, E., Bol, R., 2020. 'Co-evolution' of uranium concentration and oxygen stable isotope in phosphate rocks. Appl. Geochem. 114, 104476 https://doi.org/10.1016/j.apgeochem.2019.104476.
Tissot, F.L.H., Dauphas, N., 2015. Uranium isotopic compositions of the crust and ocean: age corrections, U budget and global extent of modern anoxia. Geochim. Cosmochim. Acta 167, 113–143. https://doi.org/10.1016/j.gca.2015.06.034.
Tissot, F.L.H., Chen, C., Go, B.M., Naziemiec, M., Healy, G., Bekker, A., Swart, P.K., Dauphas, N., 2018. Controls of eustasy and diagenesis on the 238U/235U of carbonates and evolution of the seawater (234U/238U) during the last 1.4 Myr. Geochim. Cosmochim. Acta 242, 233–265. https://doi.org/10.1016/j.gca.2018.08.022.
Tribovillard, N., Algeo, T.J., Lyons, T., Riboulleau, A., 2006. Trace metals as paleoredox and paleoproductivity proxies: an update. Chem. Geol. 232, 12–32. https://doi.org/10.1016/j.chemgeo.2006.02.012.
Vengosh, A., Cowan, E.A., Coyte, R.M., Kondash, A.J., Wang, Z., Brandt, J.E., Dwyer, G. S., 2019. Evidence for unmonitored coal ash spills in Sutton Lake, North Carolina: implications for contamination of lake ecosystems. Sci. Total Environ. 686, 1090–1103. https://doi.org/10.1016/j.scitotenv.2019.05.188.
Voigt, J., Hathorne, E.C., Frank, M., Vollstaedt, H., Eisenhauer, A., 2015. Variability of carbonate diagenesis in equatorial Pacific sediments deduced from radiogenic and stable Sr isotopes. Geochim. Cosmochim. Acta 148, 360–377. https://doi.org/10.1016/j.gca.2014.10.001.
Wallace, M.W., Hood, A.S., Shuster, A., Greig, A., Planavsky, N.J., Reed, C.P., 2017. Oxygenation history of the neoproterozoic to early phanerozoic and the rise of land plants. Earth Planet. Sci. Lett. 466, 12–19. https://doi.org/10.1016/j.epsl.2017.02.046.
Wang, Z., Hill, R., Williams, G., Dwyer, G.S., Hu, J., Schnug, E., Bol, R., Sun, Y., Coleman, D.S., Liu, X.-M., Sandstrom, M.R., Vengosh, A., 2023. Lead isotopes and rare earth elements geochemistry of global phosphate rocks: insights into depositional conditions and environmental tracing. Chem. Geol. 639, 121715 https://doi.org/10.1016/j.chemgeo.2023.121715.
Weyer, S., Anbar, A.D., Gerdes, A., Gordon, G.W., Algeo, T.J., Boyle, E.A., 2008. Natural fractionation of 238U/235U. Geochim. Cosmochim. Acta 72, 345–359. https://doi.org/10.1016/j.gca.2007.11.012.
Xu, S., Chen, M., Feng, T., Zhan, L., Zhou, L., Yu, G., 2021. Use ggbreak to effectively utilize plotting space to deal with large datasets and outliers. Front. Genet. 12.
Yuan, Y., Chen, T., Zhang, F., Liu, Y., Xiong, G., Wei, G.-Y., Dahl, T.W., Yan, W., Ling, H.-F., Cheng, H., Shen, S.-Z., 2023. Substantial incorporation of isotopically heavy reduced U species into marine carbonate sediments. Geochim. Cosmochim. Acta 358, 27–37. https://doi.org/10.1016/j.gca.2023.07.023.
Zhang, F., Lenton, T.M., del Rey, Á., Romaniello, S.J., Chen, X., Planavsky, N.J., Clarkson, M.O., Dahl, T.W., Lau, K.V., Wang, W., Li, Z., Zhao, M., Isson, T., Algeo, T.

J., Anbar, A.D., 2020. Uranium isotopes in marine carbonates as a global ocean paleoredox proxy: a critical review. Geochim. Cosmochim. Acta 287, 27–49. https://doi.org/10.1016/j.gca.2020.05.011.